ACS Photonics

Article

Cite This: ACS Photonics XXXX, XXX, XXX−XXX

In Vivo and *in Situ* Spectroscopic Imaging by a Handheld Stimulated Raman Scattering Microscope

Chien-Sheng Liao,[†,‡,§] Pu Wang,[∥] Chih Yu Huang,[⊥] Peng Lin,[#] Gregory Eakins,[□] R. Timothy Bentley,[¶] Rongguang Liang,[⊥] and Ji-Xin Cheng[*,†,‡,§]

[†]Department of Electrical and Computer Engineering, Boston University, Boston, Massachusetts 02215, United States
[‡]Department of Biomedical Engineering, Boston University, Boston, Massachusetts 02215, United States
[§]Photonics Center, Boston University, Boston, Massachusetts 02215, United States
[∥]Vibronix Inc, West Lafayette, Indiana 47907, United States
[⊥]College of Optical Sciences, University of Arizona, Tucson, Arizona 85721, United States
[#]Weldon School of Biomedical Engineering, Purdue University, West Lafayette, Indiana 47907, United States
[□]Jonathan Amy Facility, Department of Chemistry, Purdue University, West Lafayette, Indiana 47907, United States
[¶]Department of Veterinary Clinical Science, Purdue University, West Lafayette, Indiana 47907, United States

Supporting Information

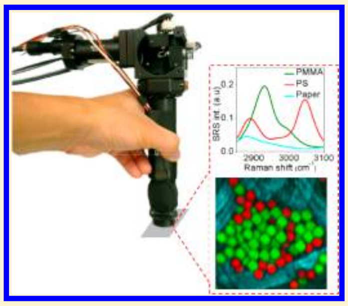

ABSTRACT: Spectroscopic stimulated Raman scattering (SRS) microscopy is a label-free technique that generates chemical maps of live cells or tissues. A handheld SRS imaging system using an optical fiber for laser delivery will further enable *in situ* and *in vivo* compositional analysis for applications such as medical diagnosis and surgical guidance. In fiber-delivered SRS, the interaction of two ultrashort pulses in the confined mode area creates a significant background that overwhelms the stimulated Raman signal from a sample. Here, we report the first background-free fiber-delivered handheld SRS microscope for *in situ* chemical imaging. By temporally separating the two ultrafast pulses propagating in the fiber and then overlapping them on a sample through a highly dispersive material, we detected a stimulated Raman signal that is 200 times weaker than the background induced by the fiber. Broad applications of the handheld SRS microscope were demonstrated through *in situ* ambient-light chemical mapping of pesticide on a spinach leaf, cancerous tissue versus healthy brain tissue in a canine model, and cosmetic distribution on live human skin. A lab-built objective lens further reduced the size of the pen-shaped microscope to about one centimeter in diameter.

KEYWORDS: *chemical imaging, Raman spectroscopy, handheld microscope*

Coherent Raman scattering (CRS) microscopy, based on coherent anti-Stokes Raman scattering (CARS) or stimulated Raman scattering (SRS), allows high-speed visualization of chemicals in living cells or fixed tissues.[1−5] The imaging speed of CRS microscopy has reached up to video rate by focusing all laser energy into one single Raman band.[6,7] Spectroscopic CRS technologies further resolve overlapped Raman bands and identify important biomarkers in cancer cells[8,9] or generate chemical maps of tissues.[10,11] Developments of microsecond-scale SRS imaging[12−14] enabled real-time live cell imaging and label-free flow cytometry.[15] Toward the direction of cancer detection in the clinic, an intraoperative two-color SRS microscope has been reported to provide histopathological analysis of brain cancerous tissues in a surgical room.[16] A multimodal nonlinear microscope acquires optical signals, including CARS, second/third-harmonic generation, and autofluorescence, and shows promising results of label-free histopathology.[17]

In addition to these technical advances, developments of handheld microscopes or implantable endoscopes would allow *in situ* or *in vivo* imaging of an area that is inaccessible by benchtop units. Even though fiber-optic-based endoscopic imaging systems including confocal fluorescence[18] and multiphoton microscopy[19−21] have been reported to reach submicrometer resolution and real-time imaging speed, it remains a grand challenge for CRS handheld imaging systems due to various nonlinear effects induced in fibers. For the CRS process, two ultrashort laser pulses, namely, pump and Stokes pulses, are required to coherently excite molecular vibrations. The propagation of temporally overlapped pump and Stokes pulses within a confined mode area also generates a significant background originated from their interaction in a fiber, including four-wave-mixing (FWM), SRS, and cross-phase modulation (XPM).[22] This nonspecific background overwhelms the relatively weak CRS signals and degrades the chemical selectivity of CRS imaging tremendously.[23]

There has been a great effort in suppressing the background signals for CRS handheld microscopes and endoscopes.

Received: October 13, 2017
Published: December 27, 2017

DOI: 10.1021/acsphotonics.7b01214
ACS Photonics XXXX, XXX, XXX−XXX

For CARS measurements, both Raman-resonant signals from samples and the background induced by a fiber exhibit shorter wavelengths compared to excitation pulses. Thus, the background signals generated in a fiber can be eliminated by using a dichroic mirror or a filter between the fiber end and the sample.[24,25] The FWM in a fiber can also be suppressed by using pump and Stokes pulses with orthogonal polarization states when propagating in a fiber.[26] However, CARS signals are a mixture of Raman-resonant and also nonresonant signals induced by FWM of samples, which requires a sophisticated algorithm to retrieve Raman-resonant signals.[27,28] In comparison, SRS provides the same spectral profiles as spontaneous Raman. For SRS measurement, in addition to the SRS effect due to FWM in the fiber core,[29] XPM also contributes to the background because of the confined mode field in silica in fibers.[30] One approach to suppress these backgrounds is to propagate laser pulses in a hollow-core photonics crystal fiber (HC-PCF). It has been reported that no nonlinear signals were observed in an HC-PCF with a spectral coverage up to ~1000 cm^{-1},[31] limited by the narrow bandwidth of the photonics band gap of the HC-PCF. With this spectral coverage, the C═C vibration at ~1600 cm^{-1}, amide I band at ~1650 cm^{-1}, and C−H vibration at ~2850 cm^{-1}, which provide abundant information on biological samples, are not accessible.

Here, we demonstrate a time-domain approach to eliminate the nonlinear background generated in a photonic crystal fiber. We temporally separate the pump and Stokes pulses propagating in a fiber, so the interaction between the two pulses is minimized. A dispersive material after the fiber end reoverlaps the two pulses on a sample. This approach avoids any nonlinear background generated by the interaction of two temporally overlapped pulses with the fiber core. Combined with our SRS spectroscopic platform in which a few adjacent Raman bands are excited by fast tuning the temporal delay of two spectrally focused pulses,[14] we built a handheld SRS microscope that can analyze chemical contents of a sample *in situ* and *in vivo*. We detected SRS signals from olive oil at 1658 cm^{-1} of C═C and 1745 cm^{-1} of C═O vibrations, which were 200 times weaker than the nonresonant background generated in the fiber. In addition, since SRS signals are acquired from demodulation of a strong local oscillator, our handheld microscope is free from the disturbance of ambient light. We demonstrated *in situ* chemical mapping of pesticide residue on a spinach leaf under room light. We further performed spectroscopic imaging of canine brain cancerous tissue and observed spectral features of white matter, gray matter, necrosis, and cancer cells. Finally, we demonstrated handheld SRS imaging of a human inner arm *in vivo* to visualize cosmetic distribution on the skin.

■ RESULTS

Background-Free Handheld Stimulated Raman Microscope. Our setup is composed of two parts: spectroscopic excitation and a handheld microscope, as depicted in Figure 1. The spectroscopic excitation part (Figure 1a) is published in our previous work[14] and described in detail in the Methods. In the handheld microscope (Figure 1b), a large-area PCF (LMA-20, NKT Photonics) with a length of ~1.8 m is used to deliver pump and Stokes pulses to the sample. This fiber has been used to show low spectral broadening for picosecond pulses.[24] A lens with a 50 mm focal length collimates both beams after the PCF. The two pulses then propagate in a 40 mm SF-11 rod three times with the aid of two right-angle prisms attached to the surface of the glass rod. The total 120 mm traveling distance in an SF-11 rod results in a 5.32 ps temporal mismatch between 887 and 1040 nm pulses, calculated by

$$\frac{120\ \mathrm{mm}}{c/n_{\mathrm{a}}(887\ \mathrm{nm})} - \frac{120\ \mathrm{mm}}{c/n_{\mathrm{a}}(1040\ \mathrm{nm})} = 5.32\ \mathrm{ps} \qquad (1)$$

where n_{g} is the group refractive index, $n_{\mathrm{g}}(887\ \mathrm{nm}) = 1.7995$, and $n_{\mathrm{g}}(1040\ \mathrm{nm}) = 1.7862$. Importantly, this mismatch enables temporal overlap of two pulses on a sample while being completely separate in the fiber. The combined pulses are then scanned by two galvo mirrors to form an image. An objective (20×, Olympus) is used to focus laser light on the sample. A 1 mm thick BK-7 window is used to fix the focal plane on the surfaces of samples. The backscattered photons are collected by the same objective. Since the polarization states of backscattered photons are scrambled, a polarizing beam splitter reflects part of the backscattered photons to the photodiode on which a filter (980sp, Chroma) blocks the modulated 1040 nm beam. A home-built resonant circuit on a 0.5 in. × 1 in. printed circuit board selectively amplifies the 2.4 MHz signals and

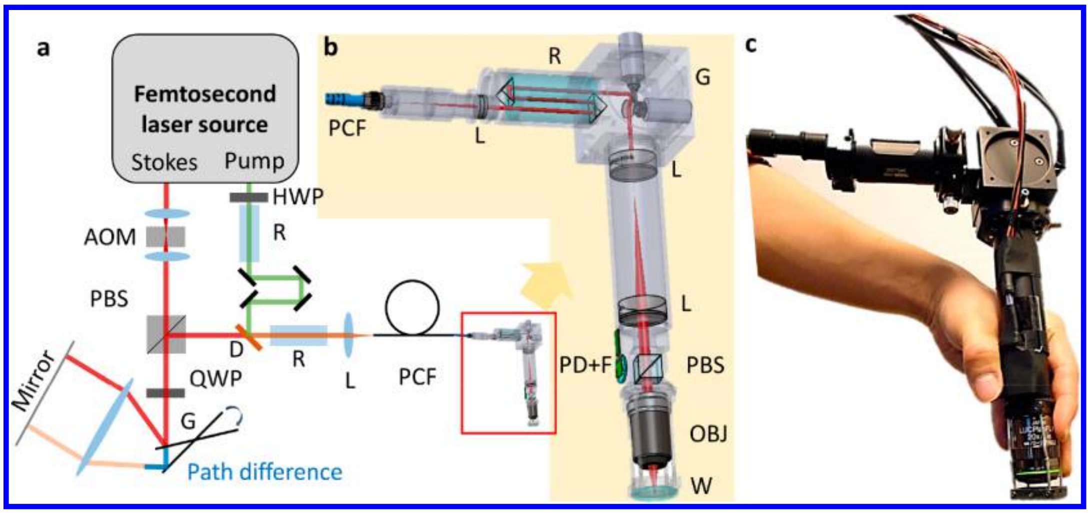

Figure 1. Experimental design. (a) Excitation. (b) Handheld microscope. (c) Digital image of the handheld microscope. AOM: acousto-optical modulator; D: dichroic mirror; F: filter; G: galvo mirror; HWP: half waveplate; L: lens; OBJ: objective; PBS: polarizing beam splitter; PCF: photonics crystal fiber; PD: photodiode; QWP: quarter-wave plate; R: rod (SF-11); W: window.

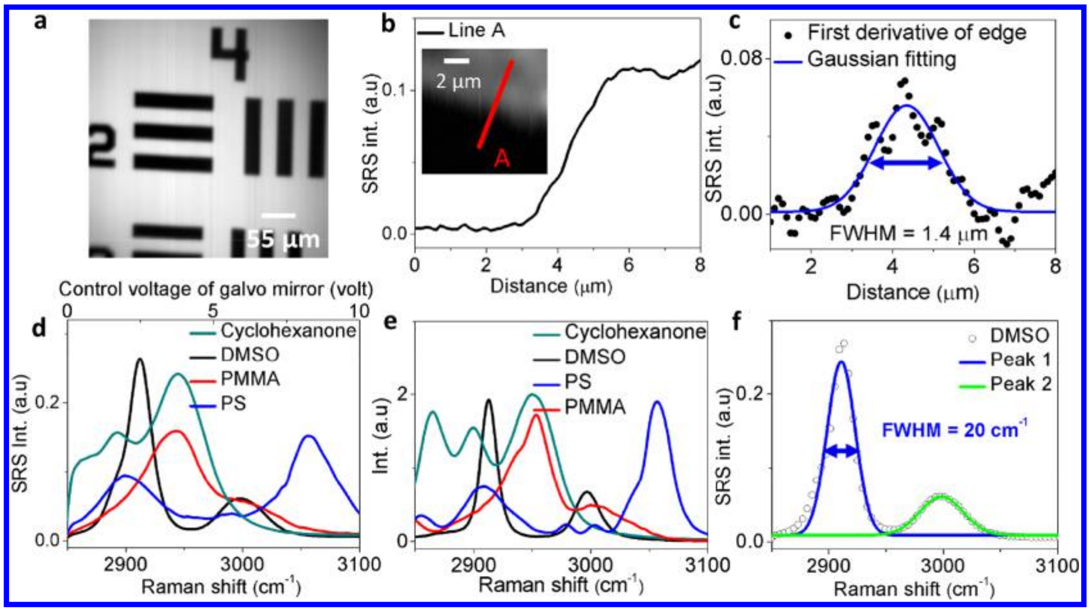

Figure 2. Characterization. (a) Reflectance image of a resolution target showing a field of view of ∼0.38 × 0.38 mm^2. (b) SRS profile of DMSO at the interface of a gold edge. (c) First derivative of (b) and Gaussian fitting. (d) SRS spectra of standard chemicals. (e) Spontaneous Raman spectra of standard chemicals. (f) Spectral resolution tested by DMSO.

outputs the signal to a lock-in amplifier (HF2LI, Zurich). Figure 1c shows a picture of our handheld SRS microscope.

Performance of the Handheld SRS Microscope. We first characterized our handheld SRS microscope by a resolution target. A 380 μm field of view was obtained (Figure 2a), which was limited by the optics used before the objective. The spatial resolution was tested by imaging the edge of the gold coating covered with olive oil (Figure 2b). Gaussian fitting of the first derivative of the intensity profile across the gold edge showed a full-width at half-maximum of ∼1.4 μm (Figure 2c). We further confirmed the spectral fidelity by comparing SRS spectra acquired with our system (Figure 2d) to spontaneous Raman spectra (Figure 2e). A spectral coverage of ∼200 cm^{-1} was obtained, determined by the spectral bandwidth of femtosecond pump and Stokes pulses. We then characterized the spectral resolution by the known Raman peak of a DMSO solution at 2912 cm^{-1}. Considering the inherent bandwidth of this Raman band of 13 cm^{-1} and the measured 20 cm^{-1} bandwidth, our spectral resolution was estimated to be ∼15 cm^{-1} (Figure 2f).

To demonstrate real-time hyperspectral SRS imaging, we scanned a sample of mixed dried microspheres of polystyrene (PS) and poly(methyl methacrylate) (PMMA) (Polyscience) on a piece of paper at the speed of 8 frames per second at 2890 cm^{-1} with 200 × 200 pixels (Supplementary Figure 1a). Under this imaging speed, the hand movement induced negligible distortion to the acquired images. We diluted 5 μm PS and PMMA with pure water by 100 times, respectively, and mixed the two diluted solutions. Then a droplet of the 5 μL mixture was placed on a paper. The spectroscopic images were acquired by sequentially tuning the optical delay in each spatial line and then 200 lines in one image. A total of 200 spectra within each spatial line were acquired in 0.56 ms, and a spectroscopic image with 20 spectral points was completed within 3 s. By multivariate curve resolution (MCR) analysis (details in Methods), the chemical concentration maps of PS, PMMA, and cellulose fibers of paper indicated their spatial distributions (Supplementary Figure 1b), and the output spectra matched the spontaneous Raman data shown in Figure 2. In sum, the imaging speed at a single Raman band was 8 frames per second, which was mainly limited by the galvo mirrors for laser scanning. This speed was sufficient to reduce distortion due to hand movement. The spectroscopic imaging required less than 3 s, with a spectral resolution of 15 cm^{-1}.

Distinguishing Stimulated Raman Signals from Background Induced by a Fiber. The nonlinear background imposes a challenge on the CRS endoscope and handheld microscope. It has been reported that these backgrounds can be suppressed by using pump and Stokes pulses with orthogonal polarization states when propagating in a fiber.[26] The use of an air core of a hollow-core photonics crystal fiber has been demonstrated to reduce nonlinear signals with a spectral coverage up to ∼1000 cm^{-1}.[31] Here we completely remove the nonlinear signals induced by the pulse interaction by temporally separating the pump and Stokes pulses. To demonstrate that our design effectively eliminates the nonlinear backgrounds generated in the fiber, we acquired SRS images of olive oil and air interfaces in the C═C and C═O regions around 1656 cm^{-1} and scanned the temporal delay of the pump beam by 32 ps (Figure 3). We observed strong signals between 6.1 and 19.4 ps from both air and olive oil (Figure 3a,b). By considering the group refractive indices of the pump pulse at 887 nm and Stokes pulse at 1040 nm in silica (1.4649 and 1.4626, respectively), the 13.3 ps temporal difference between the two signal peaks corresponded to a spatial separation of 1.73 m in the PCF, which is consistent with the fiber length of ∼1.8 m used in our system. These strong signals between 6.1 and 19.4 ps with highest intensities of 8.2 were possibly contributed by the XPM at the fiber front tip (at 6.1 ps), within the fiber core (between 6.1 and 19.4 ps), and at the fiber end tip (at 19.4 ps).[32] In addition, we found two comparably weak peaks with intensities of 0.016 and 0.006 at 25.5 and 27 ps, respectively (Figure 3c), which were more than 200 times weaker than the peak from the fiber end at 25.5 ps. The image at 25.5 ps showed clear contrast between olive oil and air (Figure 3d), indicating that the signals were from the olive oil but not the fiber background. In comparison, the image at 18.7 ps presented a constant

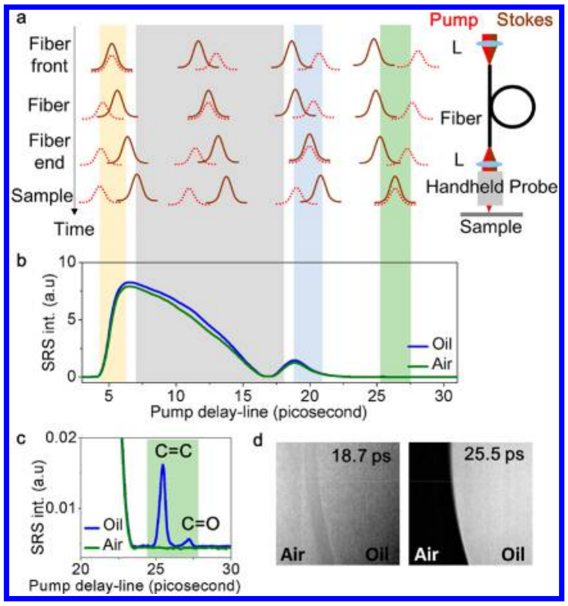

Figure 3. Elimination of the fiber background in the time domain. (a) Temporal overlap of the pump and Stokes pulses at the fiber front tip, inside the fiber, at the fiber end tip, and on the sample. (b) Spectral profiles of fiber background and Raman signals of the sample, (c) Zoom in of signals in (b). (d) Image of olive oil/air interface at 18.7 and 25.5 ps.

background from both oil and air (Figure 3d). The temporal difference of 6.1 ps between signals at 19.4 ps (fiber end) and at 25.5 ps (olive oil) was slightly larger than our calculation of 5.32 ps in eq 1, which can be contributed by the dispersion of the lens and objective. In sum, our design effectively detected the SRS signal that was more than 200 times weaker than the nonlinear signals generated in the fiber.

Mapping Pesticide Residues on a Spinach Leaf *in Situ*. The detection of pesticide residues on vegetable and fruits is essential for food safety and human health. Gas chromatography and chromatography−mass spectroscopy have been used to detect pesticide residues,[33,34] but with disadvantages of being time-consuming and labor-intensive and the complicated procedures of sample preparation. Raman spectroscopy has been demonstrated to detect pesticide on fruits *in situ* with an acquisition time of ∼1 min per spectrum.[35] Surface-enhanced Raman spectroscopy has been reported with improved acquisition speed for *in situ* detection of pesticide from fruits, on which gold nanoparticles were applied in order to enhance the weak Raman signal.[36] Our imaging platform enables visualization of pesticide residues on the surface of crop plants under ambient light. Here, we detect pesticide residue without the use of nanoparticles. We performed spectroscopic SRS imaging of a spinach leaf with pesticide residue in the molecular fingerprint region (Figure 4a). We dissolved thiabendazole, which is a systemic benzimidazole fungicide commonly used to control fruit and vegetable diseases, in DMSO and applied the solution on a spinach leaf. The solution was dried, and a thiabendazole crystal was formed on the leaf. The spinach leaf showed two-photon absorption signals[37] from chlorophyll (Figure 4b,c) with a broad spectral profile induced by cross-correlation of the pump and Stokes pulses (in green, Figure 4d), while thiabendazole exhibited a Raman signal at 1600 cm^{-1} from the aromatic ring (in red, Figure 4d). The MCR concentration map showed the distribution of thiabendazole from the spinach leaf (Figure 4e,f). These data demonstrated the capability of our device for *in situ* label-free imaging of pesticide residue on the surface of a vegetable.

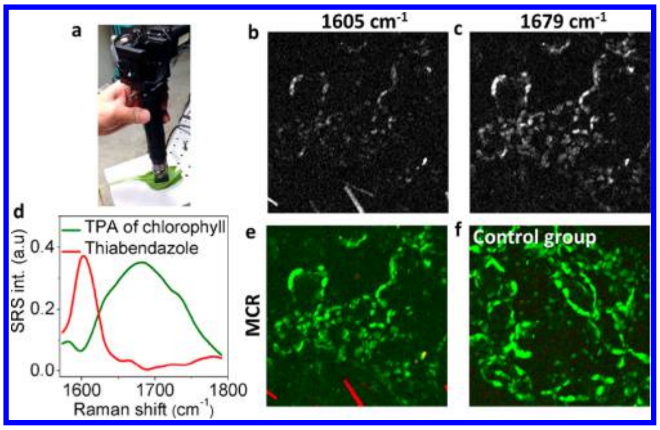

Figure 4. Spectroscopic imaging of residual pesticide on a spinach leaf. (a) Digital picture of the experimental setup. (b) SRS image at 1605 cm^{-1} of a spinach leaf. (c) SRS image at 1679 cm^{-1} of a spinach leaf. (d) MCR output spectra. (e, f) SRS concentration maps of chlorophyll and thiabendazole.

Discrimination of Brain Cancerous Tissues from Normal Tissues. For malignant gliomas, surgical resection remains the primary treatment to delay tumor recurrence and prolong survival,[38,39] but the inability to visualize invasive brain cancers leads to incomplete surgical resections and negatively affects the survival rates. A handheld microscope that detects residual cancer cells in the surgical cavity is essential for tissue-sparing surgical guidance. Toward this direction, recently a handheld contact spontaneous Raman spectroscopy probe that collects one vibrational spectrum from a 0.5 mm diameter tissue area intraoperatively within 1 s has been developed to assess the residual cancer cells in a surgical cavity with a dark environment.[40] Recently a benchtop SRS microscope has been demonstrated to image unprocessed specimens from neurosurgical patients in an operating room, with results showing remarkable concordance with conventional hematoxylin and eosin stain (H&E) histopathology.[16] A handheld SRS microscope can be potentially used to provide *in vivo* and *in situ* histopathological assessment in a surgical room. Toward this goal, we performed SRS spectroscopic imaging of healthy and cancerous brain tissue derived from a canine model. The 30 μm frozen-sectioned tissue on a slide was placed on top of a piece of paper to simulate a nontransparent bulk tissue. The samples were mounted on a 2D translational stage, and the handheld microscope was stabilized on an optical table. We scanned 400 × 400 pixels with a pixel dwell time of 6 μs. Figure 5a,b show the SRS image at 2900 cm^{-1} of healthy and tumor tissues, respectively. In healthy brain tissue, single myelinated axon fibers were clearly observed (location A, Figure 5a) with a strong CH_2 vibration at 2850 cm^{-1} due to lipid content (Figure 5c). Location B with a CH_3 signal at 2940 cm^{-1} and weaker CH_2 signals indicated enriched cell body and low lipid composition, which can be assigned to gray matter.[41] In cancerous tissue, the signal of CH_2 vibration was weaker compared to the healthy region (Figure 5c), and the spectral profiles in locations C and D matched reported SRS spectra of necrosis and tumor cells.[41] MCR analysis decomposed the white matter from gray matter in the junction region in healthy tissue (Figure 5d) and the necrotic region from a high concentration of tumor cells in the cancerous tissue (Figure 5e), with their MCR spectral profiles shown in Figure 5f. Collectively, these data show the ability of

DOI: 10.1021/acsphotonics.7b01214
ACS Photonics XXXX, XXX, XXX−XXX

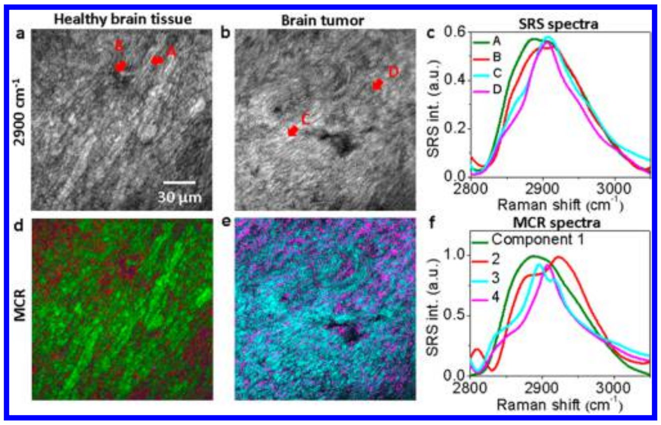

Figure 5. Spectroscopic imaging of canine healthy brain and tumor tissues. (a) SRS image at 2900 cm^{-1} of healthy brain tissue and (b) tumor tissue. (c) SRS spectra of locations indicated in (a) and (b). (d, e) MCR output concentration maps and (f) spectral profiles.

our platform to identify cancer cells from healthy tissues. This capacity would enable *in situ* tissue-sparing histopathological assessment during brain tumor surgery.

***In Vivo* Skin Imaging of Human Inner Arm.** We further demonstrated the capability of monitoring drug delivery on live human skin. Conventionally topical drug delivery is analyzed by tape-stripping or microdialysis techniques.[42] The tape-stripping approach removes a microscopic layer of stratum corneum and analyzes the concentration of the drug molecule. In the microdialysis technique, a probe is implanted superficially into the dermis or subdermis, and the drug concentration is analyzed by passive diffusion. However, these techniques are invasive and time-consuming. Real-time visualization of drug diffusion into a biological tissue *in vivo* provides a noninvasive way to assess drug delivery efficiency. Here we demonstrated *in vivo* spectroscopic imaging of human skin tissue of the inner arm before and after applying a commercially available cosmetic, which is difficult to access by a benchtop unit (Figure 6a). We scanned 200 × 200 pixels at a single Raman band with a pixel dwell time of 2 μs, corresponding to a speed of 8 frames per second (visualization 1). Then, we performed spectroscopic imaging in the spectral window of 2800−3000 cm^{-1}. Without applying any cosmetic, the SRS image at 2920 cm^{-1} only showed structures in the stratum corneum layer (Figure 6b). We further applied a commercially available cosmetic product composed of vitamin E mixed alpha tocopherol on the skin. The Raman spectrum of this cosmetic exhibited a spectral profile overlapping with the skin tissue in C−H vibrations (Supplementary Figure 2), and therefore imaging at a single Raman band of 2920 cm^{-1} provided limited contrast of this cosmetic from skin tissues (Figure 6b). MCR analysis decomposed the skin and cosmetic components based on their spectral profiles (Figure 6c). Figure 6d shows a broad coverage of cosmetic in the stratum corneum layer. After removal of excess cosmetic by lens cleaning paper, the cosmetic residue can still be observed (Figure 6d). Together, these data showed that our device is capable of mapping a specific chemical in a spectrally overlapped tissue *in vivo* on a human subject.

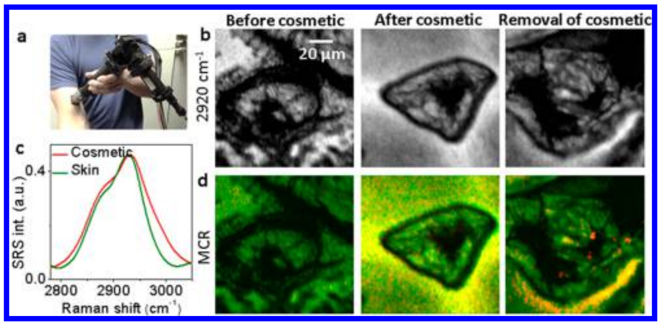

Figure 6. *In vivo* imaging of human skin tissue. (a) Skin of inner arm was used. (b) SRS image at 2920 cm^{-1} before applying cosmetic, after applying cosmetic, and after removal of excess cosmetic. (c) MCR output spectra. (d) MCR results of (b).

Miniaturized Achromatic Objective Lens for Handheld SRS Imaging. One critical step moving our handheld microscope toward clinical applications of medical diagnosis and surgical guidance is to engineer a robust and small optical probe. Here we further demonstrate the feasibility of miniaturizing our handheld microscope through the design of an achromatic miniature objective lens system. Our objective lens system is composed of four aspheric surfaces and four lenses: lens 1 and lens 3 are made from PMMA, and lens 2 and lens 4 are made from OKP-4 HT (Figure 7a,b). The chromatic aberration is carefully compensated to cover from 798 to 1040 nm, covering from low wavenumber to C−H vibrations at ~2900 cm^{-1}. The numeric aperture is 0.5, with a clear aperture of 11.0 mm and length of 15.7 mm. The size is less than half of a commercial objective with similar numeric aperture (Figure 7c). We integrate this miniature objective lens in our handheld SRS microscope (Figure 7d) and compare the performance to a commercial objective by imaging 2 μm polystyrene microspheres at 2880 cm^{-1}. A comparable signal-to-noise ratio is measured (Figure 7e). In sum, the miniaturized design of the achromatic objective lens further paves the way to clinical applications.

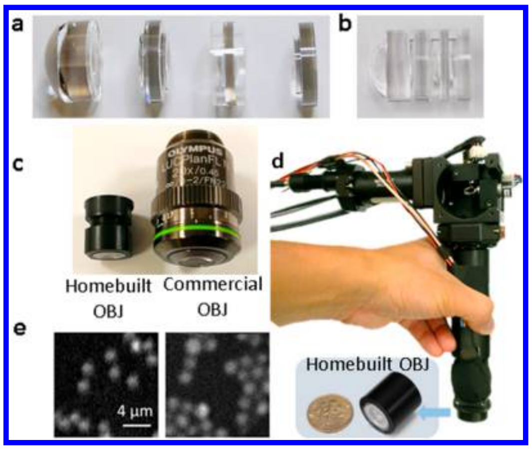

Figure 7. Design of miniaturized achromatic objective lens. (a) Individual lens and (b) the assembled objective. (c) Picture of a lab-built objective lens and commercial objective. (d) Integration of a lab-built objective lens in a handheld microscope. (e) SRS imaging of a 2 μm polystyrene microsphere by lab-built and commercial objectives.

DISCUSSION

In this work, we report a new approach to eliminate the nonresonant background induced by the interaction of two ultrashort pulses propagating in an optical fiber, which enables the development of a handheld fiber-delivered stimulated Raman microscope. Combined with our spectroscopic platform, our development enables a handheld laser scanning microscope with chemical selectivity. To overlap two ultrashort pulses in the time

DOI: 10.1021/acsphotonics.7b01214
ACS Photonics XXXX, XXX, XXX−XXX

domain after the fiber, we currently triple passed laser pulses in a 40 mm SF-11 glass rod which exhibits group refractive indices of 1.7995 and 1.7862 for 887 and 1040 nm, respectively. The refractive index difference of 0.0133 generates a 5.32 ps temporal mismatch for two ultrashort pulses after propagating in 120 mm SF-11 glass. The bulky SF-11 glass rod can be replaced with materials with higher dispersion in the near-infrared region. For example, zinc selenide, a solid compound comprising zinc and selenium, has been widely used for the near-infrared to infrared region due to its low absorption. The group refractive indices at 887 and 1040 nm are 2.6429 and 2.5742, respectively. The refractive index difference of 0.0687 induced by zinc selenide is able to reduce current optical length in SF-11 by 5.2 times. Therefore, the dimensions of our handheld microscope can be reduced by simply replacing the glass rod with a zinc selenide window. In addition, the size of the handheld microscope can be further optimized by the state-of-the-art laser steering technology. In our current design we used galvo mirrors for laser scanning in the handheld microscope, which constrained the probe size. There have been tremendous efforts in developing a miniaturized optical system for a handheld confocal microscope by microelectromechanical system devices.[43,44] A two-dimensional microelectromechanical system scanner is expected to reduce our probe size similar to the state-of-the-art handheld confocal microscope.

Currently our design acquires spectroscopic images from the surface of a sample. We demonstrated detection of pesticide residues on the surface of plants, identification of cancerous tissue from a resected sample, and visualization of a cosmetic on human skin. The development of handheld 3D spectroscopic images will further enable new applications. For example, such a device will be able to map cancer cells from the surface of a surgical cavity to ∼100 μm in depth, which will further improve the outcome of tumor resection surgery. Another example is to study the dynamics of drug penetration on live human skin. Current state-of-the-art technologies that can tune the depth of focus in a fluorescence microscope, including a deformable mirror[45] and ultrasound lens,[46] can be integrated with our handheld microscope.

■ CONCLUSION

We have developed a handheld spectroscopic SRS microscope in which a fiber delivered two laser pulses for imaging. We minimized the nonlinear effects in the fiber by temporally separating pump and Stokes pulses propagating in the fiber and overlapping them on the sample through a dispersive material. Our approach enabled detection of an SRS signal that is 200 times weaker than the nonresonant background induced by the fiber. We demonstrated *in situ* detection of pesticide residue on a spinach leaf, label-free imaging of canine cancerous brain tissue, and *in vivo* imaging of a cosmetic on live human skin, in a handheld setting and under ambient light. We also showed the feasibility of miniaturization of a handheld SRS probe by a lab-built objective lens. In future studies, we will build a transportable system with a compact laser source. Collectively, our development holds the potential of bringing an SRS microscope to a subject, thus opening a broad range of applications not accessible by a benchtop unit.

■ METHODS

Experimental Setup of Spectroscopic SRS Excitation Platform. A tunable 80 MHz pulsed laser (InSight, Spectra Physics) provides two synchronized outputs. The fixed 1040 nm beam with a ∼220 fs pulse width as the Stokes beam is first intensity-modulated by an acousto-optic modulator (Isomet) at 2.4 MHz and then directed to our delay-line tuner in which the collimated light is directed to the edge of a tilted galvo mirror and focused with a lens on a flat mirror. The retroreflected light experiences a millimeter-scale difference in optical path when the galvo mirror is scanned, as reported in our previous work.[14] Then the Stokes pulse is sent to pass through a 12.7 cm SF-11 rod. For the pump beam, the tunable output from the laser provides a spectral range from 680 to 1300 nm. The polarization of the ∼120 fs pump pulse width is rotated by a half-wave plate in order to match the polarization of the Stokes beam. Then, the pump and Stokes pulses are combined and chirped by one 12.7 cm SF-11 rod. The pulse widths of the pump and Stokes beams are stretched to 800 and 500 fs, respectively, measured with an autocorrelator (PulseScope, APE). The combined pulses are then coupled into a large-area PCF (LMA-20, NKT Photonics) with a fiber length of ∼1.8 m. This fiber has been used to show low spectral broadening for picosecond pulses.[24] The coupling efficiencies for 887 and 1040 nm are 38% and 40%, respectively. After the PCF, pump and Stokes pulses are collimated by a lens with a 50 mm focal length, sent to a 40 mm SF11 rod, and propagated for a 120 mm distance by the aid of two right-angle prisms (PS910H-B, Thorlabs) attached to the two ends of an SF11 rod. Then two galvo mirrors (6215HM60B and 671215H-1HP, Cambridge) are used to scan an image of the sample. The focal lengths of the two lenses between the galvo mirrors and the objective are 30 and 75 mm, respectively. The optical power on the sample is 40 mW for 887 nm and 40 mW for 1040 nm. The total power before fiber coupling is 350 mW for 887 nm and 250 mW for 1040 nm. The throughput of our handheld system is 11% for 887 nm and 16% for 1040 nm. After the fiber, the pulse widths of the pump and Stokes beams are stretched to 3.6 and 2 ps, respectively. Considering the spectral bandwidth of 122 cm^{-1} for a pump beam at 887 nm and 66 cm^{-1} for a Stokes beam at 1040 nm, the ratio between the pump and Stokes pulse widths should be close to 122 cm^{-1}/66 cm^{-1} = 1.8. Therefore, before coupling into the PCF, we send the Stokes beam at 1040 nm to propagate through two 12.7 cm SF-11 rods and the pump beam at 887 nm to propagate through one 12.7 cm SF11 rod. The pulse width after the LMA fiber is 3.6 ps for 887 nm and 2 ps for 1040 nm, and the ratio between the pump and Stokes pulse widths is close to 1.8. The chirped femtosecond pump and Stokes pulses focus their entire bandwidth into a narrow spectral region.[47] Therefore, each temporal delay between the chirped pump and Stokes pulses corresponds to a Raman shift. By scanning the temporal delay of one of pulses with our delay-line tuner, SRS spectroscopic imaging based on this spectral focusing scheme is performed.

Spectral Features of Protein and a Commercial Cosmetic. To identify the spectral features of a commercially available cosmetic that is mostly composed of vitamin E and human skin, which mostly exhibits protein signals, we acquired a spontaneous Raman spectrum from the cosmetic (Raphe Pharma Laboratories) and BSA (Sigma-Aldrich) (Supplementary Figure 2). In the CH vibrational region (2800−3000 cm^{-1}), the cosmetic exhibits a broader spectral profile.

Lab-Built Miniaturized Achromatic Objective Lens. The lens configuration of the microscope objective is shown in Supplementary Figure 3a. The microscope objective has an NA of 0.5. Lens 1 and lens 3 are made from PMMA, and lens 2 and lens 4 are made from OKP-4 HT. There are four aspheric surfaces in this design. Supplementary Figure 3b shows the corresponding modulation transfer function. Figure 7a shows the lens elements fabricated by a diamond turning process and the assembly objective. We can clearly see the mechanical structures outside of the lens' clear apertures that serve an assembling and aligning purpose. To simplify the lens assembling process and accuracy, we add assembling features as shown in Supplementary Figure 4. In this case, the lens' clear aperture is 11 mm, and the lens diameter including the integrated mechanical mount is 13 mm. We apply a press fit between the two lenses so that when we clip one lens onto the other, the mechanical mounts are strong enough to hold the lenses while maintaining the alignment of the lenses within the tolerance value. The step height of every mechanical mount is set to be 0.7 mm. Ideally, the step height should be large enough to hold the lens steadily. However, because we are diamond turning the mechanical mount structure and the lens surface at the same time, the maximum permissible step height is limited by the lens profile, radius of the half-radius diamond tool, and the primary clearance angle of the diamond tool.

Spontaneous Raman Spectroscopy. The spontaneous Raman spectra of targeted objects were taken by a Raman spectromicroscopy setup described previously.[48]

Multivariate Curve Resolution Analysis. We adopted multivariate curve resolution (MCR) and alternating least-squares fitting to decompose the SRS spectral images into chemical maps of the specimen, as described in our previous study.[49] MCR is a bilinear model,[50] capable of decomposing a measured spectral data set $\mathbf{D}$ into concentration profiles and spectra of chemical components, represented by matrices $\mathbf{C}$ and $\mathbf{S}^{\mathrm{T}}$, $\mathbf{D} = \mathbf{C}\cdot\mathbf{S}^{\mathrm{T}} + \mathbf{E}$. Here, $\mathbf{T}$ means the transpose of matrix $\mathbf{S}$. $\mathbf{E}$ is the residual matrix or experimental error. The inputs to MCR are the data set $\mathbf{D}$ and the reference spectra of each component. $\mathbf{S}$ contains the output spectra of all fitted components. The output concentration of a chemical component at each pixel is expressed as a percentage relative to the intensity of the MCR-optimized spectrum.

■ ASSOCIATED CONTENT

Ⓢ Supporting Information

The Supporting Information is available free of charge on the ACS Publications website at DOI: 10.1021/acsphotonics.7b01214.

Additional information (PDF)

Images of living human skin at a speed of 8 frames per second in handheld setting (MP4)

■ AUTHOR INFORMATION

Corresponding Author

*E-mail: jxcheng@bu.edu. Phone: +1 (617) 353-1276.

ORCID

Ji-Xin Cheng: 0000-0002-5607-6683

Notes

The authors declare the following competing financial interest(s): Note: J.-X.C. and P.W. have a financial interest in Vibronix Inc.

■ ACKNOWLEDGMENTS

This work was supported by Keck Foundation, NIH R21 CA182608, and R01 GM114853 to J.X.C.

■ REFERENCES

(1) Zumbusch, A.; Holtom, G. R.; Xie, X. S. Three-Dimensional Vibrational Imaging by Coherent Anti-Stokes Raman Scattering. *Phys. Rev. Lett.* **1999**, *82*, 4142−4145.

(2) Freudiger, C. W.; Min, W.; Saar, B. G.; Lu, S.; Holtom, G. R.; He, C.; Tsai, J. C.; Kang, J. X.; Xie, X. S. Label-Free Biomedical Imaging with High Sensitivity by Stimulated Raman Scattering Microscopy. *Science* **2008**, *322*, 1857−1861.

(3) Camp, C. H.; Cicerone, M. T. Chemically Sensitive Bioimaging with Coherent Raman Scattering. *Nat. Photonics* **2015**, *9*, 295−305.

(4) Cheng, J. X.; Xie, X. S. Vibrational Spectroscopic Imaging of Living Systems: An Emerging Platform for Biology and Medicine. *Science* **2015**, *350*, aaa887010.1126/science.aaa8870.

(5) Liao, C. S.; Cheng, J. X. In Situ and in Vivo Molecular Analysis by Coherent Raman Scattering Microscopy. *Annu. Rev. Anal. Chem.* **2016**, *9*, 69−93.

(6) Evans, C. L.; Potma, E. O.; Puoris' haag, M.; Côté, D.; Lin, C. P.; Xie, X. S. Chemical Imaging of Tissue in Vivo with Video-Rate Coherent Anti-Stokes Raman Scattering Microscopy. *Proc. Natl. Acad. Sci. U. S. A.* **2005**, *102*, 16807−16812.

(7) Saar, B. G.; Freudiger, C. W.; Reichman, J.; Stanley, C. M.; Holtom, G. R.; Xie, X. S. Video-Rate Molecular Imaging in Vivo with Stimulated Raman Scattering. *Science* **2010**, *330*, 1368−1370.

(8) Yue, S.; Li, J.; Lee, S. Y.; Lee, H. J.; Shao, T.; Song, B.; Cheng, L.; Masterson, T. A.; Liu, X.; Ratliff, T. L.; Cheng, J. X. Cholesteryl Ester Accumulation Induced by Pten Loss and Pi3k/Akt Activation Underlies Human Prostate Cancer Aggressiveness. *Cell Metab.* **2014**, *19*, 393−406.

(9) Li, J. J.; Condello, S.; Thomes-Pepin, J.; Ma, X. X.; Xia, Y.; Hurley, T. D.; Matei, D.; Cheng, J. X. Lipid Desaturation Is a Metabolic Marker and Therapeutic Target of Ovarian Cancer Stem Cells. *Cell Stem Cell* **2017**, *20*, 303.

(10) Ozeki, Y.; Umemura, W.; Otsuka, Y.; Satoh, S.; Hashimoto, H.; Sumimura, K.; Nishizawa, N.; Fukui, K.; Itoh, K. High-Speed Molecular Spectral Imaging of Tissue with Stimulated Raman Scattering. *Nat. Photonics* **2012**, *6*, 844−850.

(11) Fu, D.; Lu, F. K.; Zhang, X.; Freudiger, C.; Pernik, D. R.; Holtom, G.; Xie, X. S. Quantitative Chemical Imaging with Multiplex Stimulated Raman Scattering Microscopy. *J. Am. Chem. Soc.* **2012**, *134*, 3623−3626.

(12) Liao, C.-S.; Slipchenko, M. N.; Wang, P.; Li, J.; Lee, S.-Y.; Oglesbee, R. A.; Cheng, J.-X. Microsecond Scale Vibrational Spectroscopic Imaging by Multiplex Stimulated Raman Scattering Microscopy. *Light: Sci. Appl.* **2015**, *4*, e265.

(13) Liao, C.-S.; Wang, P.; Wang, P.; Li, J.; Lee, H. J.; Eakins, G.; Cheng, J.-X. Spectrometer-Free Vibrational Imaging by Retrieving Stimulated Raman Signal from Highly Scattered Photons. *Sci. Adv.* **2015**, *1*, e1500738.

(14) Liao, C. S.; Huang, K. C.; Hong, W. L.; Chen, A. J.; Karanja, C.; Wang, P.; Eakins, G.; Cheng, J. X. Stimulated Raman Spectroscopic Imaging by Microsecond Delay-Line Tuning. *Optica* **2016**, *3*, 1377−1380.

(15) Zhang, C.; Huang, K.-C.; Rajwa, B.; Li, J.; Yang, S.; Lin, H.; Liao, C.-s.; Eakins, G.; Kuang, S.; Patsekin, V.; Robinson, J. P.; Cheng, J.-X. Stimulated Raman Scattering Flow Cytometry for Label-Free Single-Particle Analysis. *Optica* **2017**, *4*, 103−109.

(16) Orringer, D. A.; Pandian, B.; Niknafs, Y. S.; Hollon, T. C.; Boyle, J.; Lewis, S.; Garrard, M.; Hervey-Jumper, S. L.; Garton, H. J. L.; Maher, C. O.; Heth, J. A.; Sagher, O.; Wilkinson, D. A.; Snuderl, M.; Venneti, S.; Ramkissoon, S. H.; McFadden, K. A.; Fisher-Hubbard, A.; Lieberman, A. P.; Johnson, T. D.; Xie, X. S.; Trautman, J. K.; Freudiger, C. W.; Camelo-Piragua, S. Rapid Intraoperative Histology of Unprocessed Surgical Specimens Via Fibre-Laser-Based Stimulated Raman Scattering Microscopy. *Nat. Biomed Eng.* **2017**, *1*, 0027.

(17) Tu, H. H.; Liu, Y.; Turchinovich, D.; Marjanovic, M.; Lyngso, J. K.; Laegsgaard, J.; Chaney, E. J.; Zhao, Y. B.; You, S. X.; Wilson, W. L.; Xu, B. W.; Dantus, M.; Boppart, S. A. Stain-Free Histopathology by Programmable Supercontinuum Pulses. *Nat. Photonics* **2016**, *10*, 534−540.

(18) Flusberg, B. A.; Cocker, E. D.; Piyawattanametha, W.; Jung, J. C.; Cheung, E. L. M.; Schnitzer, M. J. Fiber-Optic Fluorescence Imaging. *Nat. Methods* **2005**, *2*, 941−950.

(19) Rivera, D. R.; Brown, C. M.; Ouzounov, D. G.; Pavlova, I.; Kobat, D.; Webb, W. W.; Xu, C. Compact and Flexible Raster Scanning Multiphoton Endoscope Capable of Imaging Unstained Tissue. *Proc. Natl. Acad. Sci. U. S. A.* **2011**, *108*, 17598−17603.

(20) Zhang, Y. Y.; Akins, M. L.; Murari, K.; Xi, J. F.; Li, M. J.; Luby-Phelps, K.; Mahendroo, M.; Li, X. D. A Compact Fiber-Optic Shg Scanning Endomicroscope and Its Application to Visualize Cervical Remodeling During Pregnancy. *Proc. Natl. Acad. Sci. U. S. A.* **2012**, *109*, 12878−12883.

(21) Gu, M.; Kang, H.; Li, X. P. Breaking the Diffraction-Limited Resolution Barrier in Fiber-Optical Two-Photon Fluorescence Endoscopy by an Azimuthally-Polarized Beam. *Sci. Rep.* **2015**, *4*.10.1038/srep03627

(22) Singh, S. P.; Singh, N. Nonlinear Effects in Optical Fibers: Origin, Management and Applications. *Prog. Electromagn Res.* **2007**, *73*, 249−275.

(23) Saar, B. G.; Johnston, R. S.; Freudiger, C. W.; Xie, X. S.; Seibel, E. J. Coherent Raman Scanning Fiber Endoscopy. *Opt. Lett.* **2011**, *36*, 2396−2398.

(24) Balu, M.; Liu, G. J.; Chen, Z. P.; Tromberg, B. J.; Potma, E. O. Fiber Delivered Probe for Efficient Cars Imaging of Tissues. *Opt. Express* **2010**, *18*, 2380−2388.

(25) Deladurantaye, P.; Paquet, A.; Pare, C.; Zheng, H. M.; Doucet, M.; Gay, D.; Poirier, M.; Cormier, J. F.; Mermut, O.; Wilson, B. C.; Seibel, E. J. Advances in Engineering of High Contrast Cars Imaging Endoscopes. *Opt. Express* **2014**, *22*, 25053−25064.

(26) Wang, Z. Y.; Gao, L.; Luo, P. F.; Yang, Y. L.; Hammoudi, A. A.; Wong, K. K.; Wong, S. T. C. Coherent Anti-Stokes Raman Scattering Microscopy Imaging with Suppression of Four-Wave Mixing in Optical Fibers. *Opt. Express* **2011**, *19*, 7960−7970.

(27) Vartiainen, E. M.; Peiponen, K. E.; Asakura, T. Phase Retrieval in Optical Spectroscopy: Resolving Optical Constants from Power Spectra. *Appl. Spectrosc.* **1996**, *50*, 1283−1289.

(28) Liu, Y. X.; Lee, Y. J.; Cicerone, M. T. Broadband Cars Spectral Phase Retrieval Using a Time-Domain Kramers-Kronig Transform. *Opt. Lett.* **2009**, *34*, 1363−1365.

(29) Andersen, T. V.; Hilligsoe, K. M.; Nielsen, C. K.; Thgersen, J.; Hansen, K. P.; Keiding, S. R.; Larsen, J. J. Continuous-Wave Wavelength Conversion in a Photonic Crystal Fiber with Two Zero-Dispersion Wavelengths. *Opt. Express* **2004**, *12*, 4113−4122.

(30) Hook, A.; Anderson, D.; Lisak, M. Effects of Cross-Phase Modulation and Pump Depletion on Stokes Pulse Dynamics in Stimulated Raman-Scattering. *J. Opt. Soc. Am. B* **1989**, *6*, 1851−1858.

(31) Brustlein, S.; Berto, P.; Hostein, R.; Ferrand, P.; Billaudeau, C.; Marguet, D.; Muir, A.; Knight, J.; Rigneault, H. Double-Clad Hollow Core Photonic Crystal Fiber for Coherent Raman Endoscope. *Opt. Express* **2011**, *19*, 12562−12568.

(32) Lombardini, A.; Andresen, E. R.; Kudlinski, A.; Rimke, I.; Rigneault, H. Origin and Suppression of Parasitic Signals in Kagome Lattice Hollow Core Fibers Used for Srs Microscopy and Endoscopy. *Opt. Lett.* **2017**, *42*, 1824−1827.

(33) Ortelli, D.; Edder, P.; Corvi, C. Pesticide Residues Survey in Citrus Fruits. *Food Addit. Contam.* **2005**, *22*, 423−428.

(34) Liu, M.; Hashi, Y.; Song, Y. Y.; Lin, J. M. Simultaneous Determination of Carbamate and Organophosphorus Pesticides in Fruits and Vegetables by Liquid Chromatography-Mass Spectrometry. *J. Chromatogr A* **2005**, *1097*, 183−187.

(35) Zhang, P.; Zhou, X. F.; Cheng, A. Y. S.; Fang, Y. Raman Spectra from Pesticides on the Surface of Fruits. *J. Phys.: Conf. Ser.* **2006**, *28*, 7.

(36) Li, J. F.; Huang, Y. F.; Ding, Y.; Yang, Z. L.; Li, S. B.; Zhou, X. S.; Fan, F. R.; Zhang, W.; Zhou, Z. Y.; Wu, D. Y.; Ren, B.; Wang, Z. L.; Tian, Z. Q. Shell-Isolated Nanoparticle-Enhanced Raman Spectroscopy. *Nature* **2010**, *464*, 392−395.

(37) Chen, M. Y.; Zhuo, G. Y.; Chen, K. C.; Wu, P. C.; Hsieh, T. Y.; Liu, T. M.; Chu, S. W. Multiphoton Imaging to Identify Grana, Stroma Thylakoid, and Starch inside an Intact Leaf. *BMC Plant Biol.* **2014**, *14*, 175.

(38) Lacroix, M.; Abi-Said, D.; Fourney, D. R.; Gokaslan, Z. L.; Shi, W. M.; DeMonte, F.; Lang, F. F.; McCutcheon, I. E.; Hassenbusch, S. J.; Holland, E.; Hess, K.; Michael, C.; Miller, D.; Sawaya, R. A Multivariate Analysis of 416 Patients with Glioblastoma Multiforme: Prognosis, Extent of Resection, and Survival. *J. Neurosurg.* **2001**, *95*, 190−198.

(39) Keles, G. E.; Lamborn, K. R.; Berger, M. S. Low-Grade Hemispheric Gliomas in Adults: A Critical Review of Extent of Resection as a Factor Influencing Outcome. *J. Neurosurg.* **2001**, *95*, 735−745.

(40) Jermyn, M.; Mok, K.; Mercier, J.; Desroches, J.; Pichette, J.; Saint-Arnaud, K.; Bernstein, L.; Guiot, M. C.; Petrecca, K.; Leblond, F. Intraoperative Brain Cancer Detection with Raman Spectroscopy in Humans. *Sci. Transl. Med.* **2015**, *7*, 274ra19274ra19.10.1126/scitranslmed.aaa2384

(41) Lu, F. K.; Calligaris, D.; Olubiyi, O. I.; Norton, I.; Yang, W. L.; Santagata, S.; Xie, X. S.; Golby, A. J.; Agar, N. Y. R. Label-Free Neurosurgical Pathology with Stimulated Raman Imaging. *Cancer Res.* **2016**, *76*, 3451−3462.

(42) Herkenne, C.; Alberti, I.; Naik, A.; Kalia, Y. N.; Mathy, F. X.; Preat, V.; Guy, R. H. In Vivo Methods for the Assessment of Topical Drug Bioavailability. *Pharm. Res.* **2008**, *25*, 87−103.

(43) Dickensheets, D. L.; Kino, G. S. Silicon-Micromachined Scanning Confocal Optical Microscope. *J. Microelectromech. Syst.* **1998**, *7*, 38−47.

(44) Murakami, K.; Murata, A.; Suga, T.; Kitagawa, H.; Kamiya, Y.; Kubo, M.; Matsumoto, K.; Miyajima, H.; Katashiro, M. A Miniature Confocal Optical Microscope with Mems Gimbal Scanner. *Boston Transducers'03: Digest of Technical Papers, Vols 1 and 2* **2003**, 587−590.

(45) Shain, W. J.; Vickers, N. A.; Goldberg, B. B.; Bifano, T.; Mertz, J. Extended Depth-of-Field Microscopy with a High-Speed Deformable Mirror. *Opt. Lett.* **2017**, *42*, 995−998.

(46) Kong, L. J.; Tang, J. Y.; Little, J. P.; Yu, Y.; Lammermann, T.; Lin, C. P.; Germain, R. N.; Cuil, M. Continuous Volumetric Imaging Via an Optical Phase-Locked Ultrasound Lens. *Nat. Methods* **2015**, *12*, 759−762.

(47) Hellerer, T.; Enejder, A. M. K.; Zumbusch, A. Spectral Focusing: High Spectral Resolution Spectroscopy with Broad-Bandwidth Laser Pulses. *Appl. Phys. Lett.* **2004**, *85*, 25−27.

(48) Slipchenko, M. N.; Le, T. T.; Chen, H. T.; Cheng, J. X. High-Speed Vibrational Imaging and Spectral Analysis of Lipid Bodies by Compound Raman Microscopy. *J. Phys. Chem. B* **2009**, *113*, 7681−7686.

(49) Zhang, D.; Wang, P.; Slipchenko, M. N.; Ben-Amotz, D.; Weiner, A. M.; Cheng, J. X. Quantitative Vibrational Imaging by Hyperspectral Stimulated Raman Scattering Microscopy and Multivariate Curve Resolution Analysis. *Anal. Chem.* **2013**, *85*, 98−106.

(50) de Juan, A.; Tauler, R. Multivariate Curve Resolution (Mcr) from 2000: Progress in Concepts and Applications. *Crit. Rev. Anal. Chem.* **2006**, *36*, 163−176.

DOI: 10.1021/acsphotonics.7b01214
ACS Photonics XXXX, XXX, XXX−XXX